Zhang, Qingcheng; Zhao, Junping; Wu, Yechao; Li, Jun; Jin, Huile; Zhao, Shiqiang; Chai, Lulu; Wang, Yahui; Lei, Yong; Wang, Shun:

Rapid and controllable synthesis of nanocrystallized nickel-cobalt boride electrode materials via a mircoimpinging stream reaction for high performance supercapacitors

Original published in:	Small. - Weinheim : Wiley-VCH. - 16 (2020), 39, art. 2003342, 13 pp.
Original published:	2020-08-28
ISSN:	1613-6829
DOI:	10.1002/smll.202003342
[*Visited:*	2021-06-02]

NANO · MICRO small
www.small-journal.com

Rapid and Controllable Synthesis of Nanocrystallized Nickel-Cobalt Boride Electrode Materials via a Mircoimpinging Stream Reaction for High Performance Supercapacitors

Qingcheng Zhang, Junping Zhao, Yechao Wu, Jun Li, Huile Jin, Shiqiang Zhao, Lulu Chai, Yahui Wang, Yong Lei, and Shun Wang**

Nickel-cobalt borides (denoted as NCBs) have been considered as a promising candidate for aqueous supercapacitors due to their high capacitive performances. However, most reported NCBs are amorphous that results in slow electron transfer and even structure collapse during cycling. In this work, a nanocrystallized NCBs-based supercapacitor is successfully designed via a facile and practical microimpinging stream reactor (MISR) technique, composed of a nanocrystallized NCB core to facilitate the charge transfer, and a tightly contacted Ni-Co borates/metaborates (NCB_i) shell which is helpful for OH^- adsorption. These merits endow NCB@NCB_i a large specific capacity of 966 C g^{-1} (capacitance of 2415 F g^{-1}) at 1 A g^{-1} and good rate capability (633.2 C g^{-1} at 30 A g^{-1}), as well as a very high energy density of 74.3 Wh kg^{-1} in an asymmetric supercapacitor device. More interestingly, it is found that a gradual in situ conversion of core NCBs to nanocrystallized Ni-Co (oxy)-hydroxides inwardly takes place during the cycles, which continuously offers large specific capacity due to more electron transfer in the redox reaction processes. Meanwhile, the electron deficient state of boron in metal-borates shells can make it easier to accept electrons and thus promote ionic conduction.

1. Introduction

The ever-growing energy demands and deteriorating environmental situations call for green and more sustainable energy storage systems. Among them, supercapacitors have attracted high attention owing to their advantages of high power density, fast charge/discharge capability, long cyclic lifespan, and good operational safety.[1–4] However, the low energy density of commercial supercapacitors has impeded their applications in energy storage devices. For this reason, many battery-type "pseudocapacitors" have been developed with the aim of boosting energy densities, including such as heteroatom-doped carbon,[5–7] transition metal compounds,[8–10] and their hybrids.[11,12] Recently, intensive research works have been focused on the studies of transition metal oxides and hydroxides as ideal pseudocapacitive materials[13–17] for supercapacitors, due to their large theoretical capacitances. However, these transition metal oxides and hydroxides usually have low electronic conductivity and large volume changes during redox reaction processes, thus leading to poor electrochemical stability.[18] Later on, researchers found that metal borides can largely improve the capacitive performance, either by indirect coating them on the surfaces of transition metal oxides and hydroxides or by direct using them as pseudocapacitive materials.[19,20] It is worth to note that metal borides possess attractive characteristics for supercapacitor applications, including high hardness, abundant active sites for redox reactions, good electron acceptors and excellent electronic properties.[21,22] More recently, Zhu and his co-workers[23] have revealed that binary-transition metal borides can achieve a synergistic effect of each component and provide affluent redox actions occurring at different potentials, indicating that bimetallic borides are expected to demonstrate improved electrochemical performances than those of monometallic borides.

Most of the above-mentioned works are largely relied on a conventional synthetic strategy, that is, conventionally mixing the reactants and precipitate in a stirred tank reactor (STR). The precipitation stage involves fast nucleation kinetics, whose characteristic timescales are always at the same magnitude or

Dr. Q. C. Zhang, Dr. J. P. Zhao, Dr. Y. C. Wu, Dr. J. Li, Dr. H. L. Jin, Dr. S. Q. Zhao, Dr. L. L. Chai, Dr. Y. H. Wang, Prof. S. Wang
College of Chemistry and Materials Engineering
Wenzhou University
Zhejiang 325035, China
E-mail: shunwang@wzu.edu.cn
Dr. Q. C. Zhang, Dr. H. L. Jin, Prof. S. Wang
Institute of New Materials and Industrial Technology
Wenzhou University
Wenzhou, Zhejiang 325025, China
Prof. Y. Lei
Fachgebiet Angewandte Nanophysik
Institut für Physik & IMN MacroNano
Technische Universität Ilmenau
Ilmenau 98693, Germany
E-mail: yong.lei@tu-ilmenau.de
The ORCID identification number(s) for the author(s) of this article can be found under https://doi.org/10.1002/smll.202003342.

DOI: 10.1002/smll.202003342

smaller than the timescale of the mixing process. Therefore, a rapid micromixing process is essential for the generation of uniform spatial concentration distribution and supersaturation level, and consequently maintaining good product quality (morphology, size distribution, purity and etc.).[24,25] However, it is difficult to achieve a rapid micromixing in STR due to its poor mixing and mass transfer performance.[26] Local supersaturation in STR is generated after the slow addition of $NaBH_4$ into metal salts solution, and then vanishes through vigorous stirring. It is neither spatially nor temporally "constant" when a droplet of $NaBH_4$ is added into STR, in which precipitates and dissolved ions have already coexisted. Especially when the reactant is pumped into STR quickly, the homogenization of solutions can be overwhelmed by the fresh reactant with a distinct feed rich zone, and hence precipitation may have already occurred or completed before the reactants accomplish homogeneous mixing.[27,28] As a consequence, the metal borides formed in STR may differ significantly from each other regarding the morphologies, sizes, microstructures, and supercapacitive performances. In addition, STR usually leads to the formation of amorphous metal borides,[29–31] which is also evidenced by the control experiments in this study. The amorphous metal borides have been reported to be less conductive than its crystallized phases and easily oxidized to loosely contacted metal borates layers, which can induce the structure collapse and the worsening of interfacial conductivity.[32,33]

To solve these problems, we have recently constructed a microimpinging stream reactor (MISR) for intensifying the micromixing behaviors of the reactant streams.[34] It is found that the nanocrystallized metal borides were successfully formed via MISR. And more importantly, an amorphous shell of metal borates was simultaneously produced and tightly covered on the core of nanocrystallized metal borides. Guo and co-workers demonstrated that the metal borates shells can protect the metal borides core structure in a stable state and hence extend the cycle life of supercapacitors.[19] MISR composes of two steel capillaries (the inner diameter = 0.6 mm) connected with a commercial T-junction (its geometrical structure is shown in Figure S1, Supporting Information), but no capillary is connected to the T-junction outlet, which provides a big-sized outlet channel to achieve a normal pressure within the T-junction chamber and also reduce the blockage problem significantly during the precipitation. Two reactant streams are ejected along the same axis in the opposite direction and collide halfway within the T-junction chamber at rapid velocities, thus creating a high energy dissipation region for the intensified micromixing and uniform supersaturation level.[34] Such a confined micro-impinging zone also ensures better process controlling of spatial concentration distribution, providing a more homogeneous and steady environment for both the precipitation and the subsequent aging processes, since the precipitates downward into another container immediately for aging treatment after the instantaneous nucleation within the T-junction chamber (the residence time < 1 s). Therefore, MISR is expected to be a powerful process intensification technology for the controllable synthesis of metal borides in high throughout production because of its bigger geometric dimensions, faster stream flow rates and negligible blockage problem as compared to conventional microchannel reactors.[35,36]

In this work, MISR was applied to synthesize a unique nanocrystallized NCB core to facilitate the charge transfer, and a tightly encapsulated NCB_i shell to advance OH^- adsorption, as shown in **Figure 1**. The as-prepared NCB@NCB_i (NCB-2, precipitated with 0.2 mol L^{-1} KBH_4 in MISR at Re_j = 4740) displayed a large specific capacity (966 C g^{-1} at 1 A g^{-1}) and good rate capability (633.2 C g^{-1} at 30 A g^{-1}), as well as a very high energy density of 74.3 W h kg^{-1} in asymmetric supercapacitor device. In addition, effects of the KBH_4 concentration, inlet jet Reynolds number (Re_j) and reactor type on the morphologies, microstructures, and supercapacitive performances of the NCB@NCB_i were studied in detail. Ni-Co hydroxide (NCOH) was also prepared using a similar MISR route and investigated as a controllable supercapacitor electrode material for comparison.

2. Results and Discussion

2.1. Structural and Morphological Characterizations of Different Materials

The chemical structures of NCB-2 and NCOH were examined by XRD analysis, as shown in **Figure 2**a. A single broad peak centered at 45° suggested the amorphous or nanocrystalline structure of NCB-2, in which the latter was confirmed by our TEM measurements. With regards to NCOH, the diffraction peaks at 19.1°, 33.4°, and 38.2° were accordance with the (001), (100), (101) plane of $Ni(OH)_2$ phase (JCPDS no. 14-0117), respectively. The slight shift of diffraction peaks could be ascribed to the introduction of Co component.

FT-IR spectra of NCB-2 and NCOH are shown in Figure 2b. Both samples displayed absorption bands located at ≈3440 and 1630 cm^{-1}, which were attributed to the O–H stretching vibration and O–H bending vibration of molecular water in the material structure, respectively.[37] It was found that two distinct peaks appeared at 1390 and 1113 cm^{-1} in NCOH, which suggested the existence of residual NO_3^- and SO_4^{2-} intercalated in the $Ni_xCo_y(OH)_2$ framework layer, respectively. However, these two peaks were invisible in the FT-IR spectrum of NCB-2, whose characteristic bands appeared at 1283 and 1408 cm^{-1} resulting from the B–O stretching vibration of oxy-functional groups on boron lattice.[38] In addition, the characteristic peaks in the region of 640–550 cm^{-1} could be assigned to the M–B vibration (M = Co, Ni) or M–O vibration.[18,39]

The thermal behaviors of NCB-2 and NCOH were studied by thermogravimetric analysis coupled with mass spectrometry. Unlike NCOH that underwent three endothermic peaks with overall weight loss of 41.1% (Figure S2a, Supporting Information), only a sharp desorption peak with a weight loss of 5.49% was observed for NCB-2 in the temperature range of 50–250 °C (Figure S2b, Supporting Information), which was attributed to the vaporization of physically absorbed H_2O. There was no negatively charged anion intercalated in the NCB-2 domains, which is corresponded reasonably well with the FT-IR spectrum in Figure 2b. The TG-MS analysis demonstrated a good thermal stability of NCB-2. In order to accurately determine its structure, portion of the NCB-2 was calcined in an Ar atmosphere at 400 °C for 3 h yield the annealed composite, which

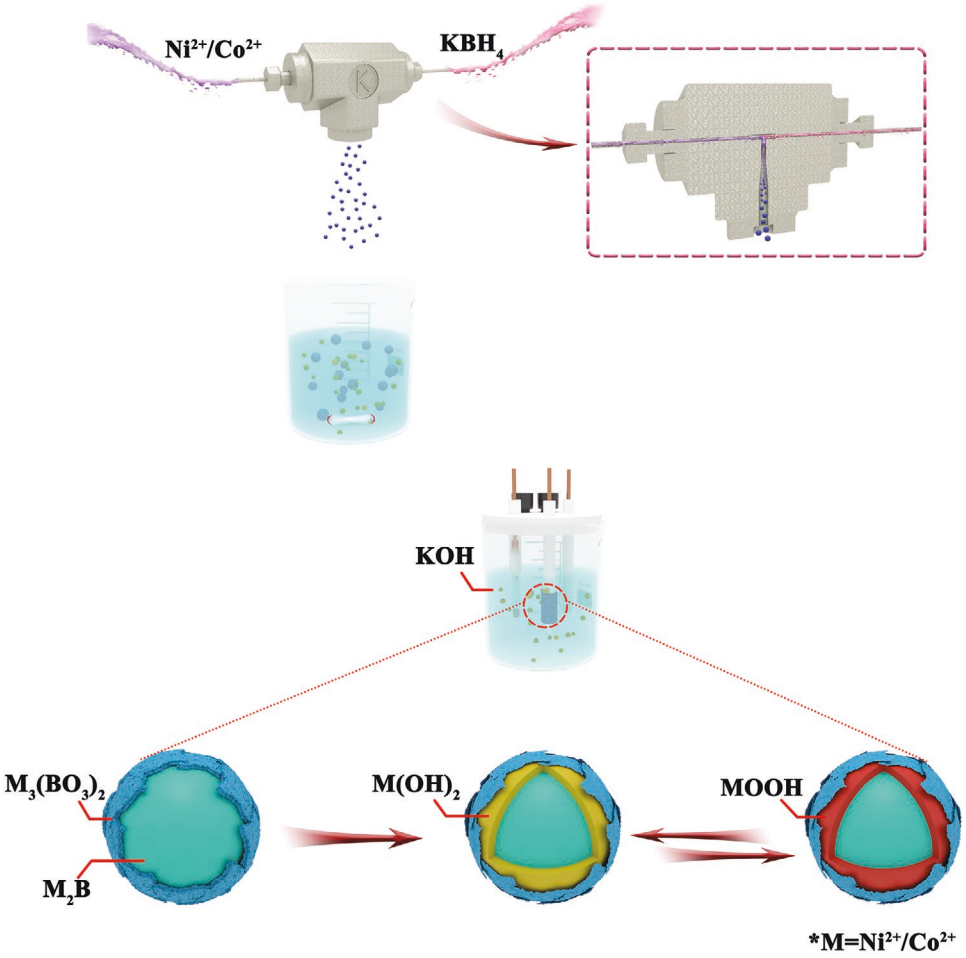

Figure 1. Sketch of synthesis and conversion of NCBs during the Faradaic redox reactions.

was denoted as "NCB-400". NCB-400 displayed a sharp XRD peak at 45.7° that between the standard diffraction lines of Ni_2B and Co_2B (Figure S3, Supporting Information), therefore, it was plausible to assume that NCB-2 was Ni-Co borides, and an annealing treatment at 400 °C would further improve the crystallinity of nanocrystalline Ni-Co borides.

XPS measurements were performed to further characterize the superficial chemical state and chemical composition of NCB-2, as shown in Figure 2c–e. The peak with the binding energy of 188.0 eV for the B1s could be ascribed to metal boride (M-B, M = Ni, Co), which was positively shifted by about 1.0 eV as compared to the elemental B (187.0 eV), suggesting an electron transfer from the alloying B to the vacant d-orbital of metallic Co/Ni making the former electron deficient while the latter enriched with electron.[40] In addition, the two peaks at 191.8 and 192.6 eV were assigned to oxidized boron originated from BO_2^- and BO_3^{3-} group, respectively (Figure 2c).[41] Therefore, the oxidized boron species were in predominance on the shell of NCB-2, which might be derived from the partly oxidation of surface metal borides upon exposure to air since oxygen was more electro-negative than boron.[42] The Ni 2p spectrum (Figure 2d) displayed major $2p_{3/2}$ peak at 856.7 eV and $2p_{1/2}$ peak at 874.6 eV, accompanied by two satellite peaks at the higher binding energy side of the Ni $2p_{3/2}$ and $2p_{1/2}$ edge, which was ascribed to the oxidized species (Ni^{2+} and Ni^{3+}) in the surface nickel borate/metaborate (denoted as Ni-B_i). In addition, the characteristic peaks at 853.1 and 870.6 eV could be assigned to the Ni—B bonding in Ni_2B.[43] Similarly, the Co $2p_{3/2}$ spectrum (Figure 2e) also showed two major peaks at 782.3 and 798.8 eV, as well as two satellite peaks, which were attributed to oxidized Co^{2+} and Co^{3+} species from cobalt borate/metaborate (denoted as Co-B_i), while the fitting peaks at 778.3 and 794.0 eV were derived from the Co—B bonding in Co_2B.[44] Therefore, the above XPS results demonstrated that NCB-2 contained metal borides and multiple oxidized metal borides, which could afford enough electro-active sites for redox reactions and thus a superior electrochemical performance was expected.

The morphologies of NCB-2 and NCOH were observed with electron microscopy. As shown in Figure S4 (Supporting Information), flake-like morphology was observed for NCOH. The NCB-2 possessed the grain morphology consisted of aggregated particles of 20–30 nm in diameter and displayed core–shell nanostructure with an outer shell of about 1.8 nm in thickness (**Figure 3**a,b). Unlike most reported amorphous structure of NCBs synthesized by the reduction method, the corresponding

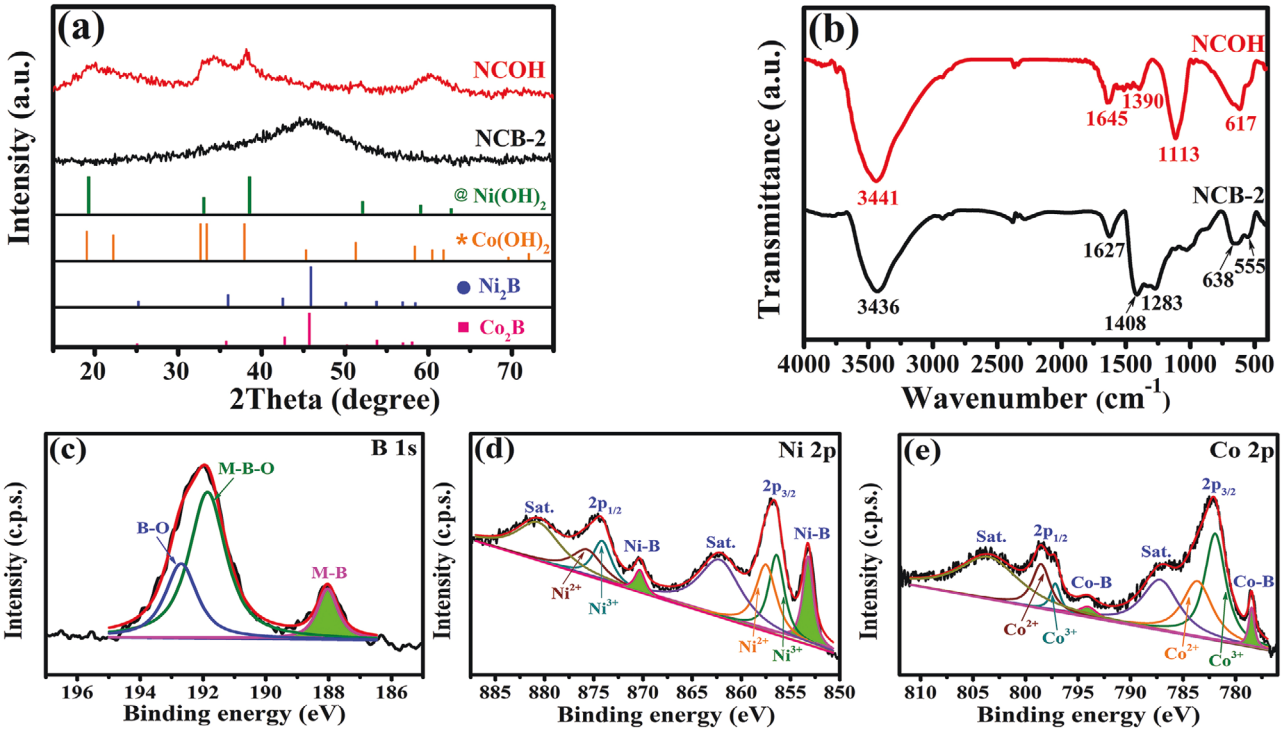

Figure 2. a) XRD patterns of NCB-2 and NCOH; b) FT-IR spectra of NCB-2 and NCOH; c) B 1s, d) Ni 2p, e) Co 2p spectra for NCB-2.

HR-TEM image of MISR-prepared NCB-2 showed low-resolution lattice fringes of 0.198 nm that were close to the standard value of 0.1976 nm for (211) plane of Ni_2B or the standard value of 0.1983 nm for (211) plane of Co_2B (using M_2B instead of Ni_2B/Co_2B as their lattice dimensions are very close) suggested the nanocrystalline property of NCB-2, which was also confirmed by its broad and diffuse halo ring in the selected-area electron diffraction (SAED) pattern (Figure 3c). This result

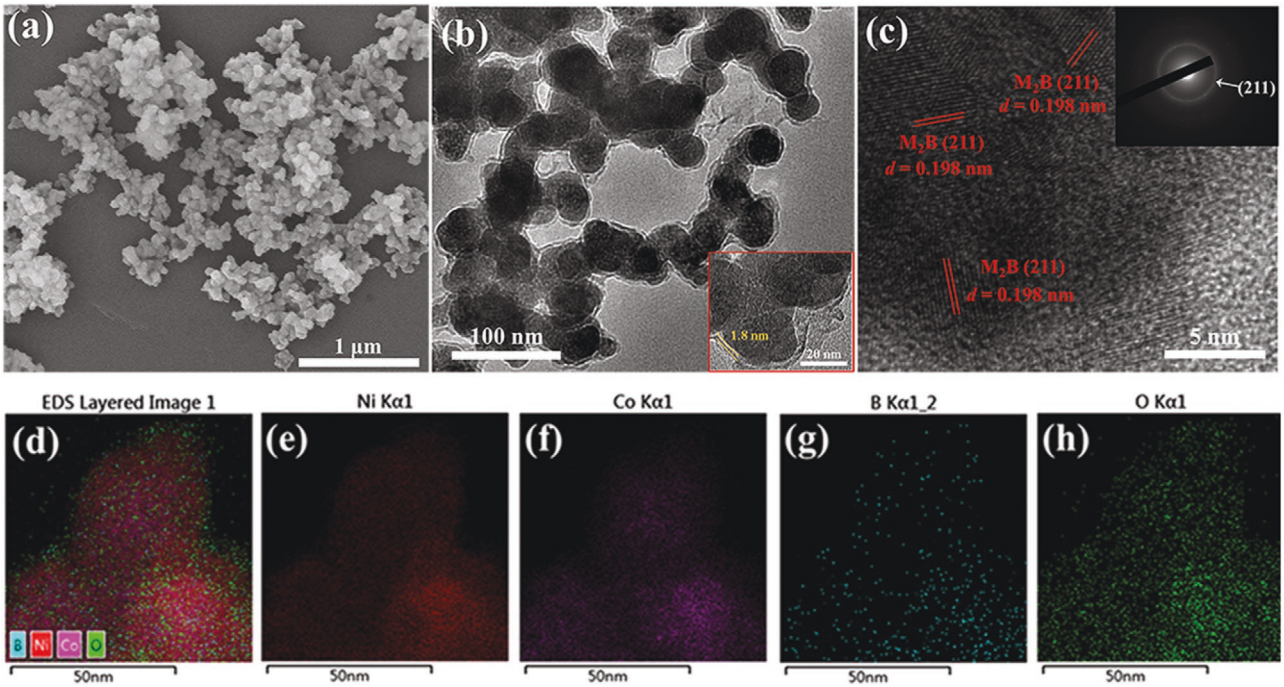

Figure 3. a) SEM image of NCB-2; b) TEM image of NCB-2; c) HR-TEM image with SAED pattern (inset) of NCB-2; d–h) EDS mapping of different elements in NCB-2.

suggested that high-velocity impinging endows the material crystallinity, which was correlated with the recent fundamental breakthrough which suggested the enhanced crystal growth using polyelectrolyte solutions and shear flow.[45] After annealing treatment at 400 °C, the HR-TEM image of NCB-400 showed that the core region consisted of well-resolved lattice fringe of 0.198 nm that matched well with the (211) plane of M_2B (Figure S5, Supporting Information). However, the shell region of NCB-400 was dim gray without discernible lattice fringe, which could be assigned to amorphous NCB_i shell,[19,46] since Ni, Co, B, and O elements could be clearly found homogeneously distributed on the shell in the EDS mapping of NCB-2 (Figure 3d–h).

2.2. Effects of KBH_4 Concentration, Inlet Jet Reynolds Number and Reactor Type on the Morphologies and Microstructures of Ni-Co Borides

The NCBs were synthesized by the chemical reduction of Ni^{2+}/Co^{2+} and KBH_4 solutions in MISR. KBH_4 acted not only as the reducing agent, but also as the boron source at the same time. The possible reaction mechanism was briefly expressed as follows (using M^{2+} instead of Ni^{2+}/Co^{2+} to simplify the equations)[30,33]

$$2M^{2+}(aq)+4BH_4^-(aq)+9H_2O(l)\rightarrow M_2B(s)+12.5H_2(g)+3H_3BO_3(aq) \quad (1)$$

$$BH_4^-(aq)+2H_2O(l)\xrightarrow{M_2B}BO_2^-(aq)+4H_2(g) \quad (2)$$

$$M^{2+}+2BO_2^-(aq)\rightarrow M(BO_2)_2(s) \quad (3)$$

It had been already discussed that in the MISR process, the mixing and nucleation were completed in a very short time and followed by a separate aging process, which provided a better control of spatial concentration distribution and hence the effect of KBH_4 concentration on the as-prepared NCBs could be clearly discussed. In the synthesis process, the total concentration of M^{2+} was 0.1 mol L^{-1} with varying KBH_4 concentration (C_K) from 0.1 to 0.3 mol L^{-1}, and the volumetric flow ratio of the two streams was kept at 1. When the metal salts mixed with KBH_4 solution, M_2B would be instantaneously precipitated according to the Reaction (1). In addition, it was reported that the as-prepared M_2B could also catalyze hydrolysis of KBH_4 to BO_2^- that subsequently precipitated with M^{2+} to form $M(BO_2)_2$ (Reactions (2) and (3)).[46,47] The formation of M_2B (Reaction (1)) was the major reaction, whose reaction kinetics might be much quicker than the Reactions (2) and (3). Therefore, once M^{2+} was reduced to form M_2B, the above Reaction (2) could be accelerated to produce the BO_2^- around the newly formed M_2B nanoparticles, followed by compounding with residual M^{2+} to form $M(BO_2)_2$ surrounding the M_2B nanoparticles to evolve into the core–shell structured $NCB@NCB_i$.[46,47] It was found that outer shell of 1.8 and 4.5 nm in thickness for NCB-2 (Figure 3b) and NCB-3 (precipitated with 0.3 mol L^{-1} KBH_4, Re_j = 4740, shown in **Figure 4**b) was controllably synthesized via MISR processes and quite sensitive to the C_K, which suggested the Reaction (2) was accelerated with an increase of C_K and this result was in accordance with the reported studies.[19,46] On the other hand, when the C_K was 0.1 mol L^{-1}, the KBH_4 was insufficient to generate M_2B particles according to the Reaction (1). However, after

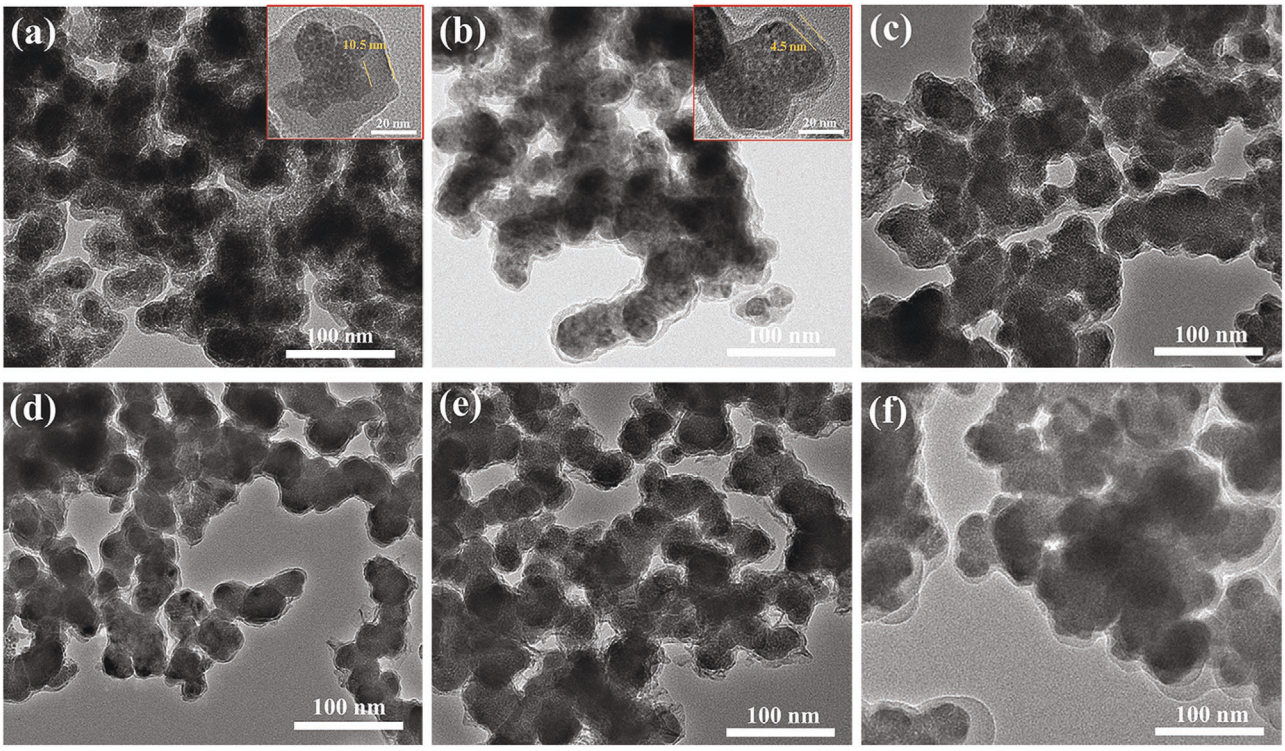

Figure 4. a–f) TEM images of NCB-1, NCB-3, NCB-4, NCB-5, NCB-6, and NCB-S, respectively.

complete consumption of B^{4-}, the excess of M^{2+} might slowly hydrolyze with H_3BO_3 to produce amorphous $M_3(BO_3)_2$ covered on the surface of M_2B particles (see Reaction (4)). It was difficult to control the hydrolysis reaction, therefore, irregular core–shell structure consisted of M_2B core and multilayer $M_3(BO_3)_2$ shell with a thickness of ≈10 nm was observed for NCB-1 (Figure 4a).

$$3M^{2+}(aq) + 2H_3BO_3(aq) \rightarrow M_3(BO_3)_2(s) + 6H^+ \quad (4)$$

It is known that the XPS analysis has a high range of sensitivities to structures on the outermost surface of the solid (outer few nanometers) but is lack of sensitivities to the structures on the deep layers of core. Therefore, the outer layer thickness of core–shell structure could also be determined by the XPS analysis, as shown in Figure S6 (Supporting Information). It was found that the intensities of Ni-B bonding, which was mainly originated from the Ni_2B in the core, increased and then decreased when the C_K was increased from 0.1 to 0.3 mol L^{-1}. This result suggested that core–shell NCB-1 possessed the thickest outer shell, followed by the NCB-3, with NCB-2 the thinnest, which correlated well with the TEM images (Figures 2b and 4a,b). The obvious difference among these approaches was attributed to the amount of KBH_4 across the reaction, because the generation of metal borides and metal borate/metaborate competed with each other. In addition, it was generally suggested that a higher reactant concentration favored the development of supersaturation as well as the crystal growth,[48] as a consequence, the crystallinity of as-prepared NCB were generally improved with an increase of C_K (Figure S7, Supporting Information). The N_2 adsorption/desorption isotherms of NCB-2 displayed a mesoporous structure with a narrow peak at 3–4 nm (Figure S8, Supporting Information), and the BET surface areas were observed to be 16.7, 27.5, and 20.4 m^2 g^{-1} for NCB-1, NCB-2, NCB-3, respectively (Figure S9, Supporting Information). Therefore, C_K played a key role on the morphologies, chemical compositions and structures of NCB composites. A higher C_K generally favored the development of supersaturation and nucleation of metal borides, however, an excess KBH_4 would also strengthen the crystal growth and produce a thick layer of NCB_i on the surface of NCB; conversely, an excess M^{2+} would slowly hydrolyze with H_3BO_3 to generate a large amount of amorphous metal borates.

Taking C_K = 0.2 mol L^{-1} as the optimal KBH_4 concentration, the NCBs were also synthesized in MISR at Re_j = 1580, 3160, and 6320, which were denoted as NCB-4, NCB-5, and NCB-6, respectively, and that NCB composite synthesized in STR was denoted as NCB-S. The crystallinity of broad peak at around 45° for the as-prepared NCBs increased when the Re_j was increased from 1580 to 6320 (Figure S10, Supporting Information), and the low-resolution lattice fringes of 0.198 nm were absent for NCB-S and NCB-4 but present in the NCB-2 and NCB-5 which suggested the nanocrystalline property of the latter two (Figure S11, Supporting Information). In addition, compared to those synthesized in MISR at high Re_j (5000 > Re_j > 3000), NCB-S and NCB-4 both displayed bigger, irregular and aggregated core–shell nanostructure with thicker shell and smaller BET surface areas of 18.9 and 15.5 m^2 g^{-1}, respectively (Figure 4c,f and Figure S12, Supporting Information). Such a phenomenon could be traced back to the different operating mode and micromixing performance of two reactors. As discussed earlier, the Reaction (1) and the Reaction (2) could be regarded as parallel competing reaction system that competed for M^{2+} to produce M_2B and $M(BO_2)_2$, respectively. If the micromixing was quick enough, the injected M^{2+} would instantaneously precipitate with B^{4-} according to Reaction (1); conversely, if micromixing was slow, a large amount of $M_3(BO_3)_2$ or $M(BO_2)_2$ could be generated since M^{2+} further reacted with BO_2^- or hydrolyze with H_3BO_3 according to Reactions (3) and (4), respectively. However, the poor micromixing and mass transfer performance of STR would lead to uneven spatial concentration distribution which resulted in a large amount of metal borate/metaborate.[49] Second, all precipitated particles remained in contact with their mother liquid for the whole precipitation process, the uneven local supersaturation was also the driving force of particle growth and agglomeration as the droplets of precipitating agents might be adsorbed on particle surface to form larger aggregates and thicker shell.[50,51] Third, in the range of Re_j below 2000, the impinging of two reactant flows in MISR was not formed completely which also resulted in a poor micromixing and uneven local supersaturation in the nucleation environment,[34] and thus bigger, irregular and aggregated particles were formed in the STR and the one synthesized in MISR at Re_j = 1580 (Figure 4c,f). For comparison, at the range of Re_j > 3000, the impinging between the two reactant streams in MISR was fully developed to achieve a very quick micromixing,[34] and the reacted precipitates flow downward into another container immediately after precipitation process, which provided a more homogeneous and steady environment for both the nucleation and aging processes on the top of its better process control and the separate aging treatment; Secondly, the increased turbulent kinetic energy at the mixing zone provided the high driving force for the mixing of two shear flow that enhanced the crystallinity of NCBs,[45] thus smaller and more uniform core–shell nanostructure with nanocrystallized NCB core and thinner NCB_i shell were synthesized in MISR at Re_j = 3160 and 4740 (Figures 4d and 3b). However, our previous study found that nearly perfect micromixing efficiency was obtained in a MISR at the Re_j range from 3000 to 5000.[34] When the Re_j was further increased to 6320, the reacted precipitated might be collided into the opposite flow due to the huge driving force from two reactant streams, which also resulted in bigger and aggregated core–shell nanostructures (Figure 4e). Therefore, the optimal Re_j range in MISR should be set to 3000–5000.

2.3. Electrochemical Measurements of NCB and NCOH Composites

The electrochemical performances of NCB-2 and NCOH were investigated by cycling voltammetry (CV) and galvanostatic charge-discharge (GCD) curves in a three-electrode configuration. As shown in **Figure 5**a, the CV curves of NCB-2 displayed a pair of strong and clearly separated oxidation and reduction peaks, indicating faradaic redox behavior of battery-type capacities.[52,53] With the increasing of scanning rate from 2 to 50 mV s^{-1}, both the oxidation and reduction peak currents

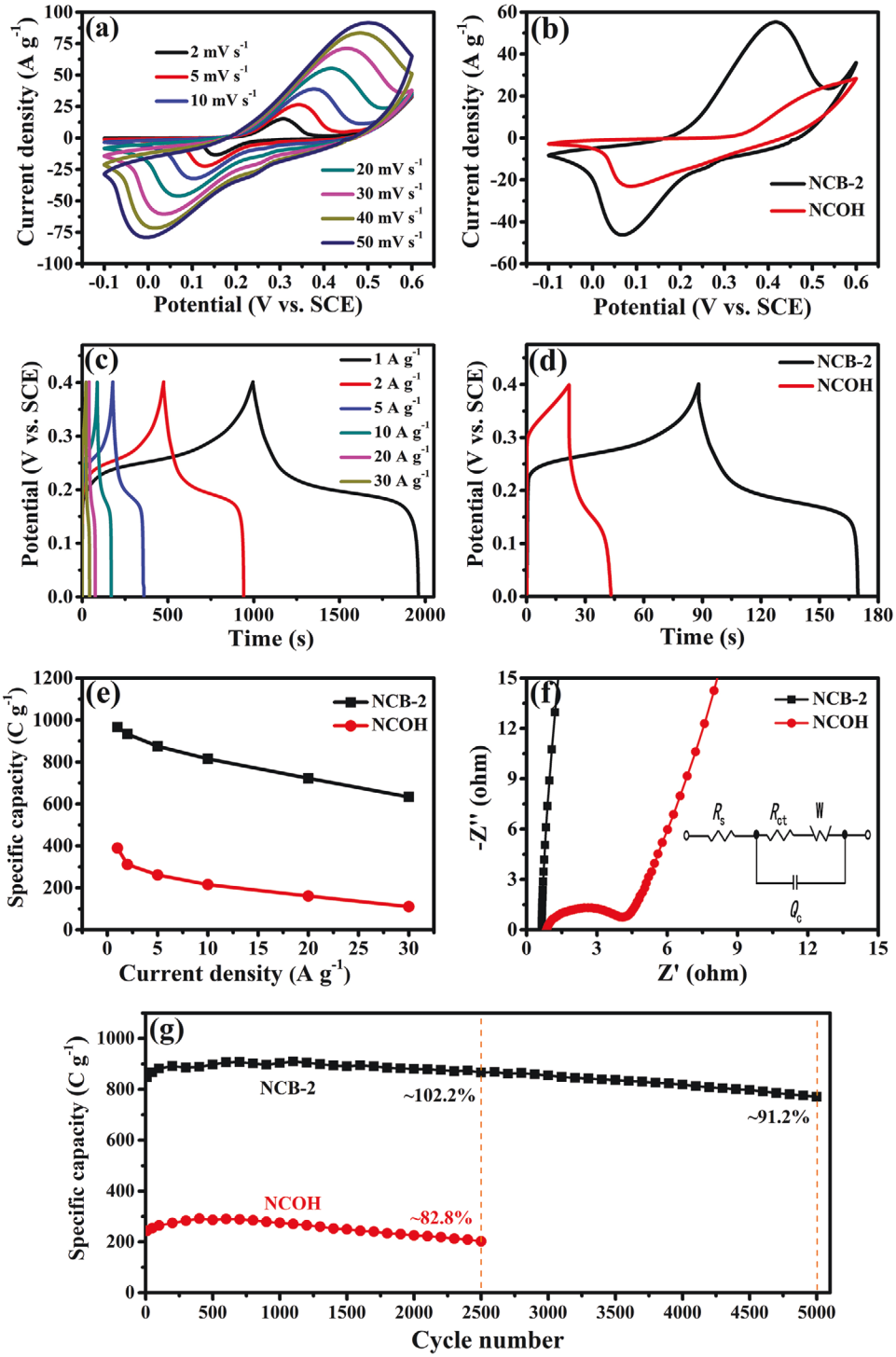

Figure 5. a) CV curves of NCB-2 at various scan rates; b) CV curves of NCB-2 and NCOH at 20 mV s^{-1}; c) GCD curves of NCB-2 at different current densities; d) GCD curves of NCB-2 and NCOH at a current density of 10 A g^{-1}; e) mass-specific capacities of NCB-2 and NCOH at different current densities; f) EIS Nyquist plots of NCB-2 and NCOH; g) cycling performances of NCB-2 and NCOH at 5 A g^{-1}.

increased but the shapes changed little for NCB-2 (Figure 5b). For comparison, the oxidation peak of NCOH disappeared when the scanning rate was slightly increased to 20 mV s^{-1}, which suggested much inferior reversibility of fast charge–discharge responses of NCOH electrode than that of NCB-2.[54,55] The GCD curves shown in Figure 5c,d further characterized the supercapacitive behaviors of NCB-2 and NCOH electrodes. Almost symmetric charge-discharge curves with obvious plateaus were seen within NCB-2 electrode, suggesting its high Coulombic efficiency and good reversibility of battery-type

capacities.[52,53] It could be calculated from the Equation (7) that at the current density of 1 A g^{-1}, NCB-2 and NCOH possessed specific capacities of 966 C g^{-1} (capacitance of 2415 F g^{-1}) and 389.2 C g^{-1} (973.3 F g^{-1}), respectively. When the current density was increased to 10 A g^{-1}, the plateau disappeared and only 215 C g^{-1} of specific capacity was retained for NCOH electrodes. This was probably because that a large current density limited ion migration into all the internal pores, thus leading to a low utilization of the electro-active materials. For comparison, by increasing the current densities to 2, 5, 10, and 20 A g^{-1}, the specific capacities of NCB-2 were 932.8, 885.2, 815.2, and 722 C g^{-1}, respectively. The GCD curve shape of NCB-2 changed little with capacity retention of 74.8% when the current density was increased from 1 to 20 A g^{-1}. Even at a high density of 30 A g^{-1}, the NCB-2 electrode still delivered a high capacity of 633.2 C g^{-1} (1583 F g^{-1}), displaying much larger capacity and superior rate capability than those of NCOH electrode.

Measurement of electrochemical impedance spectroscopy (EIS) was conducted in the frequency range from 0.001 Hz to 100 kHz to further analyze the several resistance behaviors of electrode materials. The circuit diagram fitted with the Nyquist plot that was shown in Figure 5f, it was known that the intersection of curves on the real axis Z' was the equivalent series resistance of the electrode (R_s), while the charge transfer resistance (R_{ct}) of the electrodes was represented by the diameter of the semicircle at the high-frequency region.[56] The R_s values of two electrodes were very close to 0.7–0.8 Ω since they were experimented in the same electrolyte, however, the NCB-2 displayed much smaller charge transfer resistance (R_{ct} = 0.16 Ω) than that of NCOH (R_{ct} = 3.34 Ω) electrode, suggesting a high electrical conductivity and fast electron transport throughout of the NCB-2 electrode system. This result further highlights the advantages of nanocrystallized NCB core on promoting the charge transfer. The Warburg impedances (W) of these electrodes could be predicted by the steep curves at low-frequency region. It was found that the NCB-2 electrode displayed a nearly vertical line at the low-frequency region, indicating facile electrolyte ion diffusions to electrode materials owing to large amounts of mesopores existed among the interconnected particles. Additionally, the $M(BO_2)_2$ shell was also suggested to be helpful for the adsorption of electrolyte ion on the electrode surface,[19] hence the NCB-2 electrode could remain outstanding specific capacity and rate capability. For comparison, the phase angle of Nyquist plot was close to 60°, suggesting a sluggish ion diffusion of NCOH electrode.

The cyclic stability is another important merit for the supercapacitor in practical applications. Figure 5g showed the long cycling stabilities of the above two electrodes at the current density of 5 A g^{-1}. It was found that the specific capacities of both electrodes gradually increased within the first 200 charge-discharge cycles which might due to the complete activation of electrode materials after electrolyte ions penetrated into the microscale structures.[57] However, the specific capacity of NCOH was dramatically decreased and only 82.8% of the initial capacity was retained after 2500 cycles. The apparent capacity decay of NCOH might be attributed to the increased intrinsic resistance arising from the change of the morphology and structure, or the partial delamination of electrode materials from the substrates during the fast charge-discharge process. In contrast, NCB-2 remained as high as 102.2% of initial capacity after 2500 cycles, and it still maintained at 91.2% over the 5000 charge-discharge cycles, which displayed a gratifying capacity, rate-capability and cyclic stability that outperformed most of the Ni-Co hydroxides or borides in literatures (Table S1, Supporting Information). The enhanced supercapacitive performance of NCB-2 should be attributed to its typical core–shell nanostructures as well as the intimate electrical connection between nanocrystallized NCB core and amorphous NCB_i shell, which built a reliable conductive network for fast electron transport throughout the electrode and provided adequate electroactive sites to participate in the Faradaic redox reaction. It was suggested that the introduction of boron would provide higher density of valence electrons and enhance the intrinsic conductivity, while NCB_i shell were suggested to be helpful for adsorption of OH^- and stabilization of core's structure in alkaline electrolyte.[19,58] It was found in Figures S13 and S14 (Supporting Information) that, all the amorphous NCB-1, NCB-4, and NCB-S, or highly crystallized NCB-3 and NCB-6 were consisted of irregular core–shell nanostructures and much thicker shell, displayed lower specific capacities as compared to those of nanocrystallized NCB-2 and NCB-5. Therefore, a suitable C_K, fast micromixing and uniform spatial concentration distribution were indispensable for the formation of rational core–shell nanostructures and high-performance NCB electrode materials.

2.4. Structural and Morphological Characterizations of Cycled NCB-2

The electrochemical measurement of the NCB-2 electrode by continuous charge-discharge cycling induced substantial changes in the chemical state of the constituent elements. The XRD pattern showed that Ni-Co hydroxides were formed after cycle test, coupled with the diffraction peaks of Ni-Co borides (**Figure 6**a). It was found that cycled-NCB retained most of its nanoparticle morphology without obvious volume expansion, however, the thickness of outer shell decreased (Figure 6b). Discernable lattice fringes suggested the gradually changed compositions from outside core to the center, NiOOH, CoOOH, and Ni-Co hydroxides were mostly observed around the particle shell, while metal borides appeared in the center region of the core (Figure 6c–g). In this scenario, a gradual in situ conversion of core NCBs to Ni-Co (oxy)-hydroxides inwardly took place during the charging/discharging cycles (Figure S15, Supporting Information), which continuously offered large specific capacity due to more electron transfer in the redox reaction processes. In addition, the M—B bonding (188.0 eV), Ni—B bonding (853.1 eV), and Co—B bonding (778.3 eV) disappeared after the cycle test (Figure S16a–c, Supporting Information), presumably due to the partial conversion of metal borides to metal (oxy)-hydroxide during the Faradaic redox reactions.[59,60] It is worth to note that BO^{2-} and BO_3^{3-} groups were still maintained after cycling, indicating the maintained NCB_i shell was not only helpful for OH^- adsorption, but also maintaining the gradually changed core structure in a stable state, although the intensity of oxy-boron signal in XPS spectrum was reduced and the thickness of outer shell was decreased (Figure S16c, Supporting Information),

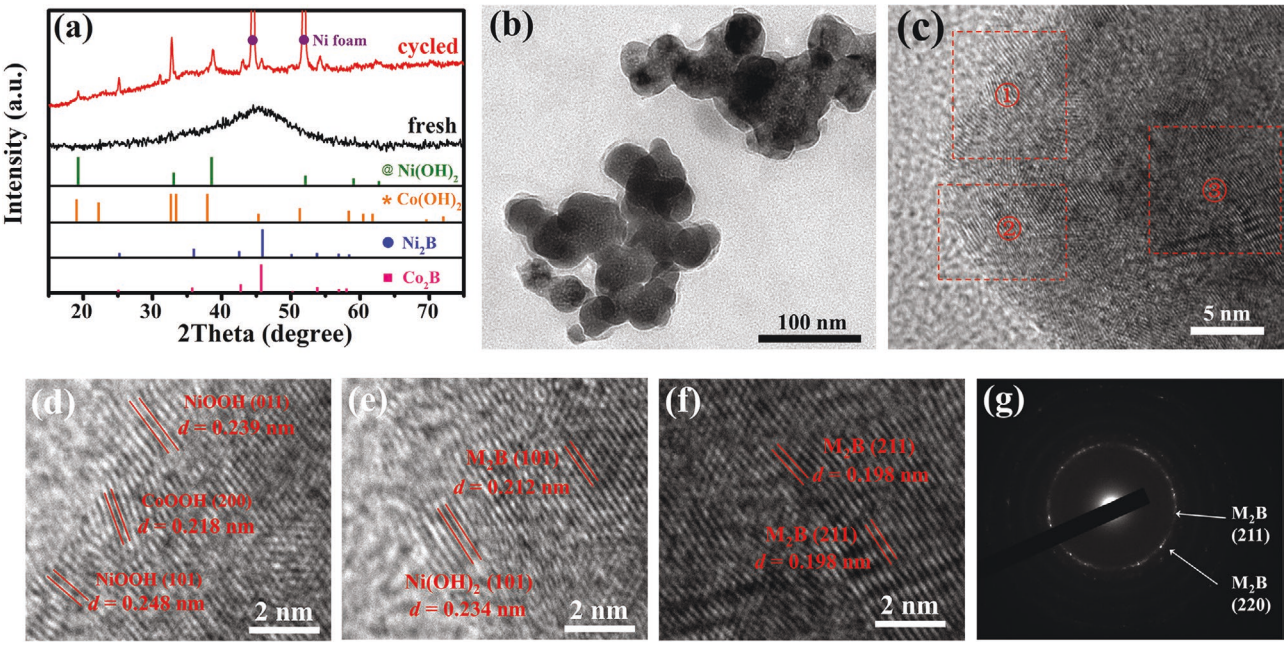

Figure 6. a) XRD patterns of NCB-2 before and after 5000 cycles test; b) TEM image of cycled NCB-2; c) HR-TEM image of cycled NCB-2; d–f) the expand view of section ①, ②, ③, respectively; g) SAED pattern of section ③.

accompanied by a decrease of B content from 25.4% to 5.8% (Table S2, Supporting Information), indicating a partial dissolution or depletion of superficial boron from the structure of NCB@NCB_i during the fast charge-discharge process, which was similar to the situation of metal borides during the OER or water splitting.[61,62] The O 1s spectrum showed the main O 1s peak shifted from 532.2 to 531.5 eV, which indicated a clear transition from the absorbed oxygen species to oxy-hydroxide species dominated within the cycled-NCB (Figure S16d, Supporting Information).[63,64] Therefore, the cycled NCB-2 was composed of a decayed but still maintained NCB_i shell, and Ni-Co (oxy)-hydroxides thin outer layer covered on the center core of nanocrystallized NCB. Similar phenomenon was also observed for the metal phosphide electrocatalysts,[65,66] for example, Stern and co-workers[66] reported the formation of an (oxy)-hydroxide shell surrounding the Ni_2P core under OER process. Therefore, it was deduced that the gradual inward transformation was occurred from the surficial metal borides core to the inside, converting to highly active oxy-hydroxide species during the continuous charge-discharge process. The generated borate-containing Ni-Co (oxy)-hydroxides outer layers accelerated the adsorption of OH^- and provided abundant active sites, while the conductive nanocrystallized Ni-Co borides core provided effective charge transfer, which ensured the excellent supercapacitive performance of NCB composites. The possible reaction mechanism of NCB could be expressed as follows (using M^{2+} instead of Ni^{2+}/Co^{2+} to simplify the equations)[19]

$$2M_2B + 20OH^- \rightarrow 4M(OH)_2 + 2(BO_3)^{3-} + 6H_2O + 14e^- \quad (5)$$

$$M(OH)_2 + OH^- \leftrightarrow MOOH + H_2O + e^- \quad (6)$$

2.5. Electrochemical Measurements of NCB//AC Asymmetric Supercapacitor

In order to evaluate the practical application of NCB-2 electrode for electrochemical energy storage, an asymmetric supercapacitor (denoted as NCB//AC, shown in Figure S18a, Supporting Information) device was assembled using NCB-2 as the positive electrode and activated carbon (AC) as the negative electrode, respectively. Figure S18b (Supporting Information) showed the CV curves of NCB//AC at different voltage windows, it was found the EDLC mechanism was operative within the voltage of 0–0.8 V, by increasing the working potential windows, the broad redox peaks were observed which suggested its battery-type capacitive property originated from the NCB-2 electrode. However, a slight hump was observed at 1.6–1.8 V, corresponding to the oxygen evolution reaction on the positive electrode. Therefore, the optimal voltage window of NCB//AC device could be extended to 1.6 V. CV curves of NCB//AC within the voltage of 0–1.6 V confirmed the contributions of both EDLC and battery-type capacitances, which were originated from AC and NCB-2, respectively (**Figure 7**a). Also, the CV shapes displayed slight change with an increase of scanning rate, which suggested fast charge-discharge response for the NCB//AC device. GCD curves of NCB//AC performed in various current densities were shown in Figure 7b. It could be seen that all of GCD curves were nearly symmetrical, indicating an ideal capacitive characteristics and good reversibility of Faradaic redox reactions. The specific capacitances evaluated from the GCD curves were 209.1, 191.2, 171.8, 139.4, 100.3, and 66.4 F g^{-1} at the current densities of 0.5, 1, 2, 5, 10, and 20 A g^{-1}, respectively, based on the total mass of the AC and NCB-2 electrode materials. Figure S18d (Supporting Information) showed the Nyquist plot of NCB//AC device, which could be calculated from the equivalent circuit

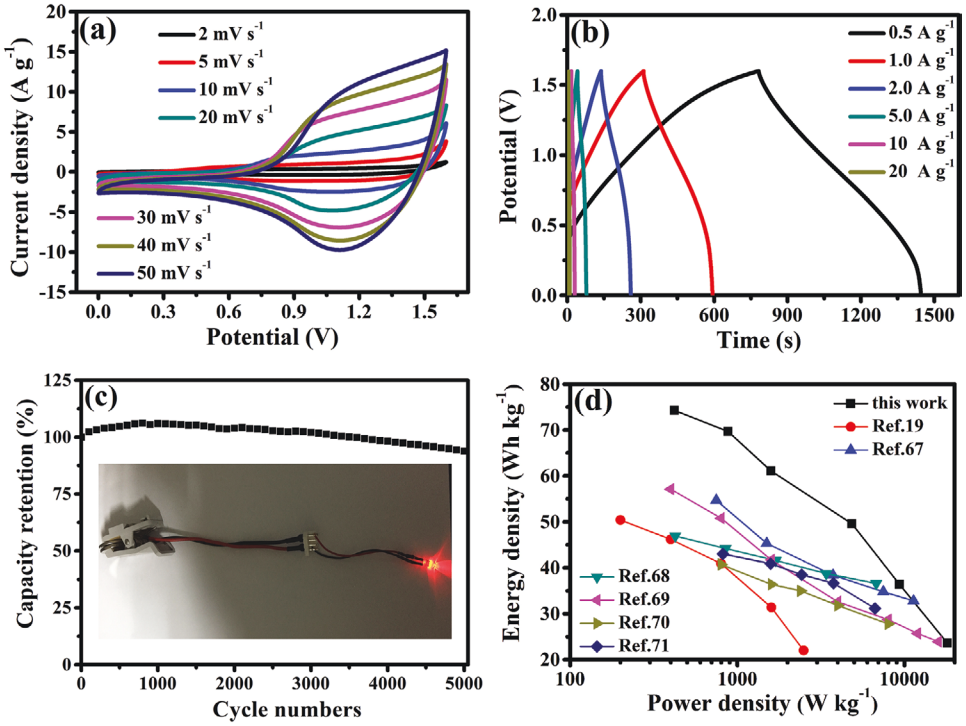

Figure 7. a) CV curves of NCB//AC device at different scanning rates; b) GCD curves of NCB//AC device at different current densities; c) Cyclic stability of NCB//AC device at 2 A g^{-1} (the inset was photograph of a red LED lighted for several minutes with two asymmetric supercapacitors in series connection); d) Ragone plot of NCB//AC device compared with those in the literatures.

that the series resistance (R_s) and charge-transfer resistance (R_{ct}) was 4.71 and 4.83 Ω, respectively. In addition, NCB//AC device displayed good cycling stability with only 6.2% capacity loss after 5000 cycles (Figure 7c). The Ragone plots describing the relationship between energy density and power density of the NCB//AC device are shown in Figure 7d. It displayed a high energy density of 74.3 Wh kg^{-1} at a power density of 420 W kg^{-1}, and still remained an energy density of 23.6 Wh kg^{-1} at a high power density of 18 076 W kg^{-1}. These values are higher than those of the previously reported Ni, Co-based composite asymmetric capacitors.[19,67–71] In addition, a red LED lighted for several minutes with two NCB//AC devices in series connection. Therefore, NCB composite was a rather promising electrode material in energy storage applications.

3. Conclusions

In this study, core–shell structured NCB@NCB_i nanoparticles (NCB-2, precipitated with 0.2 mol L^{-1} KBH_4 in MISR at Re_j = 4740) have been prepared via a rapid and controllable mircoimpinging stream reaction method, which endows the nanoparticles with unique morphologies, an unconventional nanocrystallized NCB core and a relatively stable NCB_i shell. Such designed configuration not only promotes the charge transfer attributed to the nanocrystallized NCB core, but also accelerates OH^- adsorption due to the electron deficient state of boron in NCB_i shell. These merits endow NCBs@NCB_i a large specific capacity of 966 C g^{-1} (capacitance of 2415 F g^{-1}) at 1 A g^{-1} with good rate capability and cycling stability, much superior than those of NCOH composites synthesized in the same MISR. In addition, parallel-competitive reactions between metal borides and metal borates/metaborates took place during the precipitation process, and hence a rapid micromixing and suitable KBH_4 concentration was crucial for the formation of controllable morphologies and sizes of core–shell nanostructures. It was found that an increase of KBH_4 concentration and Re_j enhanced the crystallinity of NCBs@NCB_i, while that precipitated with insufficient KBH_4, or those synthesized in reactors with slow micromixing and uneven spatial concentration distribution (STR or MISR at Re_j < 2000), all displayed bigger, irregular and amorphous core–shell nanostructures as well as much lower capacities than those in prepared in highly developed MISR (Re_j > 3000) with 0.2 mol L^{-1} KBH_4. Finally, an asymmetric supercapacitor NCB//AC was assembled with NCB-2 and activated carbon, and exhibited a high energy density of 74.3 Wh kg^{-1}, together with a high power density of 18 076 W kg^{-1} and good cycling stability. Therefore, MISR was a promising process intensification technology for the rapid production of Ni-Co borides as the high-performance supercapacitor electrode materials.

4. Experimental Section

Materials: Cobalt nitrate hexahydrate ($Co(NO_3)_2{\cdot}6H_2O$), nickel sulfate hexahydrate ($NiSO_4{\cdot}6H_2O$), potassium hydroxide (KOH), and poly tetrafluoroethylene (PTFE) were purchased from Aladdin Reagent (Shanghai) Co., Ltd. *N*-methyl-2-pyrrolidone (NMP) and potassium borohydride (KBH_4) were provided by Shanghai Macklin Biochemical Co., Ltd. Acetylene black and activated carbon (AC) (BET surface area

= 2283.4 m^2 g^{-1}) were purchased from Nanjing XFNANO Materials Tech. Co., Ltd. All the chemicals were analytical grade and used without further purification.

Synthesis of NCBs in MISR: The NCBs were synthesized through a chemical reduction method in MISR, as shown in Figure 1. A solution of $Co(NO_3)_2$ and $NiSO_4$ with a total concentration of 0.1 mol L^{-1} (molar ratio Co^{2+} : Ni^{2+} = 1:3) and a certain centration of KBH_4 solution (C_K = 0.1, 0.2, and 0.3 mol L^{-1}) as the precipitant were injected into the T-junction simultaneously with the varying volumetric flow rates ranging from 40 to 160 mL min^{-1}, which corresponded to an inlet jet Reynolds number (Re_j) ranged from 1580 to 6320 when the inner diameter was 0.6 nm. Two reactant flows impinged to each other coaxially by using two constant-flux pumps, and then downward into a beaker for further treatment. After impinging and precipitating within the T-junction under room temperature, the reacted precipitates were collected into a beaker placed in an ice water bath and then vigorously stirred for 6 h. Subsequently, the dark solids were filtered, washed with distilled water and ethanol for several times, and then freeze-dried overnight to yield nickel-cobalt borides. The obtained borides precipitated with 0.1, 0.2, and 0.3 mol L^{-1} KBH_4 in MISR at Re_j = 4740 were denoted as "NCB-1", "NCB-2", "NCB-3", respectively. In addition, the obtained borides precipitated with 0.2 mol L^{-1} KBH_4 in MISR at Re_j = 1580, 3160, and 6320 were denoted as "NCB-4", "NCB-5," and "NCB-6", respectively.

Synthesis of NCOH in MISR: NCOH was also synthesized in the similar MISR route except that aqueous ammonia (0.5% NH_3/99.5% H_2O) was chosen as the precipitant. A same mixture solution of $Co(NO_3)_2$/$NiSO_4$ and aqueous ammonia were pumped into T-junction simultaneously at a constant Re_j of 4740 and impinged each other within the T-junction chamber, then the precipitates were collected in a beaker and vigorously stirred for 6 h under room temperature to yield nickel-cobalt hydroxide (denoted as NCOH).

Synthesis of NCB in STR: NCB was also synthesized by chemical reduction method in a traditional STR. Typically, the same mixture solution of $Co(NO_3)_2$/$NiSO_4$ and as 0.2 mol L^{-1} KBH_4 solution were simultaneously dropped at 10 mL min^{-1} into a STR placed in an ice water bath. After complete adding of the solutions, the black precipitate was further vigorously stirred for 6 h. The post-processes were the same as those in MISR route, and the obtained black powder was denoted as "NCB-S".

Characterizations: Powder X-ray diffraction (XRD) analysis was employed to characterize the crystal structures of samples using X-ray diffractometer (Bruker D8) with Cu Kα radiation (λ = 0.15 406 nm). Fourier transform infrared spectra (FT-IR) were measured in the range of 4000–400 cm^{-1} using a Bruker Vetex 70 spectrometer. TG-MS analysis was performed on Netzsch STA 449F3 thermobalance coupled with a quadrupole mass spectrometer (Agilent 5975E), while the samples were heated to 1173 K at a heating rate of 5 K min^{-1}. X-ray photoelectron spectroscopy (XPS) spectra were conducted with Kratos Axis Ultradld spectrometer using Mono Al Kα radiation. The morphologies of samples were observed with scanning electron microscopy (SEM, Nova NanoSEM 200) and transmission electron microscopy (TEM, JEOL JEM-2100). High-resolution transmission electron microscopy (HR-TEM), selected area electron diffraction images and energy dispersive X-ray spectroscopy (EDX) were conducted on the same transmission electron microscopy. N_2 adsorption-desorption isotherms were recorded at 77 K using a Micromeritics apparatus (ASAP 2020M), in which all samples were pretreated in vacuum at 200 °C for 8 h, and the specific surface areas were calculated according to the Brunauer–Emmett–Teller (BET) equation.

Electrochemical Measurements: The working electrode was made by mixing 80 wt% of the as-prepared samples, 15 wt% of acetylene black and 5 wt% of poly tetrafluoroethylene (PTFE) binder in an agate mortar. Next, a small amount of N-methyl pyrrolidone (NMP) was dropped to the above mixture and ground adequately to form a homogeneous slurry, which was then uniformly smeared onto 1 cm^2 nickel foam that have been carefully pretreated with HCl solution, ethanol and acetone in sequence to remove the surface oxide layer.[72] The mass loading of the electrode material was ≈3.2 mg. The electrochemical performances were measured on an electrochemical workstation (CHI 660E, Shanghai Chenhua Co., Ltd., China) using a three-electrode configuration in 2 mol L^{-1} KOH aqueous electrolyte, with a platinum foil and a standard calomel electrode used as the counter and reference electrodes, respectively. The specific capacities (C_{sc}, C g^{-1}) and specific capacitances (C_{sp}, F g^{-1}) determined from the galvanostatic charge-discharge curves were calculated according to the Equations (7) and (8), respectively

$$C_{sc} = \frac{2 \times I \int U dt}{mU} \tag{7}$$

$$C_{sp} = \frac{2 \times I \int U dt}{mU^2 \Big|_{U_i}^{U_f}} \tag{8}$$

Where I (A) is the charge-discharge current, $\int U dt$ is the internal discharge current area, m (g) is the mass of electroactive component, U (V) is the potential with the initial and final discharge voltage of U_i and U_f, respectively.

An asymmetric supercapacitor was fabricated in a two-electrode coin-cell configuration, which is consisted of NCB-2 electrode (positive) and activated carbon (AC) electrode (negative) with one piece of cellulose acetate membrane (TF4030, NKK, Japan) as the separator sandwiched in between. According to the charge balance theory, the loading mass ratio of the positive electrode to negative electrode (m^+/m^-) was optimized to be 0.32 based on the Equation (9)

$$\frac{m^+}{m^-} = \frac{C^- \times \Delta U^-}{C^+ \times \Delta U^+} \tag{9}$$

Where m is the mass loading of electroactive material, C_{sp} is the specific capacitance, and ΔU is the potential range for the positive (+) and negative (–) electrodes, respectively.

The energy density (E, Wh kg^{-1}) and power density (P, W kg^{-1}) of the asymmetric supercapacitor were estimated from the following equations

$$E = \frac{I \int U dt}{3.6 \times m} \tag{10}$$

$$P = \frac{3600 \times E}{\Delta t} \tag{11}$$

Where C_{cell} is the coin-cell capacitance calculated from the total mass of electroactive materials coated on both the positive and negative electrodes excluding their current collectors, and Δt (s) represents the discharge time.

Supporting Information

Supporting Information is available from the Wiley Online Library or from the author.

Acknowledgements

The authors gratefully acknowledge the financial support provided by National Natural Science Foundation of China (Nos. 21706196, 51772219, 51872209, 21905208), Key Projects of Zhejiang Natural Science Foundation (Nos. LZ20E010001), Wenzhou City Public Welfare Technology Project (Nos. G20190010), and New Seeding Plan of Zhejiang Province (Nos. 2019R429062).

Conflict of Interest

The authors declare no conflict of interest.

Keywords

microimpinging stream reactors, micromixing, nanocrystallized nickel-cobalt borides, Ni-Co borides, supercapacitors

Received: May 30, 2020
Revised: July 12, 2020
Published online: August 28, 2020

[1] Y. Shao, M. F. El-Kady, J. Sun, Y. Li, Q. Zhang, M. Zhu, H. Wang, B. Dunn, R. B. Kaner, *Chem. Rev.* **2018**, *118*, 9233.
[2] Y. Shi, G. Liu, R. Jin, H. Xu, Q. Wang, S. Gao, *Carbon Energy* **2019**, *1*, 253.
[3] T. Lv, M. Liu, D. Zhu, L. Gan, T. Chen, *Adv. Mater.* **2018**, *30*, 1705489.
[4] J. Ren, Y. Huang, H. Zhu, B. Zhang, H. Zhu, S. Shen, G. Tan, F. Wu, H. He, S. Lan, X. Xia, Q. Liu, *Carbon Energy* **2020**, *2*, 176.
[5] H. Jin, J. Li, Y. Yuan, J. Wang, J. Lu, S. Wang, *Adv. Energy Mater.* **2018**, *8*, 1801007.
[6] H. Jin, X. Feng, J. Li, M. Li, Y. Xia, Y. Yuan, C. Yang, B. Dai, Z. Lin, J. Wang, J. Lu, S. Wang, *Angew. Chem., Int. Ed.* **2019**, *58*, 2397.
[7] C. Cui, Y. Gao, J. Li, C. Yang, M. Liu, H. Jin, Z. Xia, L. Dai, Y. Lei, J. Wang, S. Wang, *Angew. Chem., Int. Ed.* **2020**, *59*, 7928.
[8] W. Song, J. Wu, G. Wang, S. Tang, G. Chen, M. Cui, X. Meng, *Adv. Funct. Mater.* **2018**, *28*, 1804620.
[9] Q. Zhang, L. Tian, Y. Wu, Y. Li, L. Wen, S. Wang, *J. Alloys Compd.* **2019**, *792*, 314.
[10] K. Tao, Y. Gong, J. Lin, *Nano Energy* **2019**, *55*, 65.
[11] X. Dong, H. Jin, R. Wang, J. Zhang, J. Lu, *Adv. Energy Mater.* **2018**, *8*, 1702695.
[12] J. Zhang, H. Zhao, J. Li, H. Jin, X. Yu, Y. Lei, S. Wang, *Adv. Energy Mater.* **2019**, *9*, 1803221.
[13] H. B. Li, M. H. Yu, F. X. Wang, P. Liu, Y. Liang, J. Xiao, C. X. Wang, Y. X. Tong, G. W. Yang, *Nat. Commun.* **2013**, *4*, 1894.
[14] T. Zhai, L. Wan, S. Sun, Q. Chen, J. Sun, Q. Xia, H. Xia, *Adv. Mater.* **2017**, *29*, 1604167.
[15] N. R. Chodankar, S. Selvaraj, S. H. Ji, Y. Kwon, D. H. Kim, *Small* **2019**, *15*, 1803716.
[16] H. Liang, C. Xia, A. H. Emwas, D. H. Anjum, X. Miao, H. N. Alshareef, *Nano Energy* **2018**, *49*, 155.
[17] H. Pang, X. Li, Q. Zhao, H. Xue, W.-Y. Lai, Z. Hu, W. Huang, *Nano Energy* **2017**, *35*, 138.
[18] C. Xiang, Q. Wang, Y. Zou, P. Huang, H. Chu, S. Qiu, F. Xu, L. Sun, *J. Mater. Chem. A* **2017**, *5*, 9907.
[19] Y. Chen, T. Zhou, L. Li, W. K. Pang, X. He, Y.-N. Liu, Z. Guo, *ACS Nano* **2019**, *13*, 9376.
[20] H. Wang, J. Yan, R. Wang, S. Li, D. Brett, J. Key, S. Ji, *J. Mater. Chem. A* **2017**, *5*, 92.
[21] X. Cao, X. Wang, L. Cui, D. Jiang, Y. Zheng, J. Liu, *Chem. Eng. J.* **2017**, *327*, 1085.
[22] N. Jean Marie Vianney, G. Lanqian, D. Raksha, R. Vikas, J. Vishal, X. Bao Yu, Y. Qingyu, L. JongMin, W. Xin, *Adv. Energy Mater.* **2019**, *9*, 1901503.
[23] Q. Meng, W. Xu, S. Zhu, Y. Liang, Z. Cui, X. Yang, A. Inoue, *Electrochim. Acta* **2019**, *296*, 198.
[24] J. Baldyga, Ł. Makowski, W. Orciuch, *Ind. Eng. Chem. Res.* **2005**, *44*, 5342.
[25] H. C. Schwarzer, F. Schwertfirm, M. Manhart, H. J. Schmid, W. Peukert, *Chem. Eng. Sci.* **2006**, *61*, 167.
[26] J. Bałdyga, J. R. Bourne, S. J. Hearn, *Chem. Eng. Sci.* **1997**, *52*, 457.
[27] J. Cheng, C. Yang, Z. S. Mao, C. Zhao, *Ind. Eng. Chem. Res.* **2009**, *48*, 6992.
[28] S. Bhattacharya, S. M. Kresta, *Chem. Eng. Res. Des.* **2004**, *82*, 1153.
[29] Y. Li, B. Huang, Y. Sun, M. Luo, Y. Yang, Y. Qin, L. Wang, C. Li, F. Lv, W. Zhang, S. Guo, *Small* **2019**, *15*, 1804212.
[30] J. M. V. Nsanzimana, R. Dangol, V. Reddu, S. Dou, Y. Peng, K. N. Dinh, Z. Huang, Q. Yan, X. Wang, *ACS Appl. Mater. Interfaces* **2019**, *11*, 846.
[31] T. He, J. M. V. Nsanzimana, R. Qi, J. Zhang, M. Miao, Y. Yan, K. Qi, H. Liu, B. Xia, *J. Mater. Chem. A* **2018**, *6*, 23289.
[32] Z. Chen, X. Duan, W. Wei, S. Wang, Z. Zhang, B. J. Ni, *Nano Res.* **2020**, *13*, 293.
[33] J. Masa, P. Weide, D. Peeters, I. Sinev, W. Xia, Z. Sun, C. Somsen, M. Muhler, W. Schuhmann, *Adv. Energy Mater.* **2016**, *6*, 1502313.
[34] Z. Liu, L. Guo, T. Huang, L. Wen, J. Chen, *Chem. Eng. Sci.* **2014**, *119*, 124.
[35] T. Meincke, H. Bao, L. Pflug, M. Stingl, R. N. Klupp Taylor, *Chem. Eng. J.* **2017**, *308*, 89.
[36] Y. Yang, L. He, J. Lu, Z. Liu, N. Wang, J. Su, Y. Long, X. Lv, Y. Wen, *Electrochim. Acta* **2019**, *321*, 134673.
[37] T. Wang, S. Zhang, X. Yan, M. Lyu, L. Wang, J. Bell, H. Wang, *ACS Appl. Mater. Interfaces* **2017**, *9*, 15510.
[38] A. L. James, K. Jasuja, *RSC Adv.* **2017**, *7*, 1905.
[39] R. Chen, L. Liu, J. Zhou, L. Hou, F. Gao, *J. Power Sources* **2017**, *341*, 75.
[40] Q. Hu, G. Li, Z. Han, Z. Wang, X. Huang, X. Chai, Q. Zhang, J. Liu, C. He, *Adv. Energy Mater.* **2019**, *9*, 1970109.
[41] Y. Chen, W. K. Pang, H. Bai, T. Zhou, Y. Liu, S. Li, Z. Guo, *Nano Lett.* **2017**, *17*, 429.
[42] Z. Zhu, J. Ma, L. Xu, L. Xu, H. Li, H. Li, *ACS Catal.* **2012**, *2*, 2119.
[43] X. Chen, Z. Yu, W. Li, Z. Zhou, Y. Chen, *J. Mater. Chem. A* **2019**, *7*, 764.
[44] J. M. V. Nsanzimana, Y. Peng, Y. X. Yang, L. Thia, W. Cheng, Y. X. Bao, W. Xin, *Adv. Energy Mater.* **2018**, *8*, 1701475.
[45] J.-K. Sun, Y. I. Sobolev, W. Zhang, Q. Zhuang, B. A. Grzybowski, *Nature* **2020**, *579*, 73.
[46] T. Tan, P. Han, H. Cong, G. Cheng, W. Luo, *ACS Sustainable Chem. Eng.* **2019**, *7*, 5620.
[47] W. J. Jiang, N. Shuai, T. Tang, Q. H. Zhang, J. S. Hu, *Angew. Chem.* **2017**, *56*, 6572.
[48] H. C. Schwarzer, W. Peukert, *AIChE J.* **2004**, *50*, 3234.
[49] D. L. Marchisio, L. Rivautella, A. A. Barresi, *AIChE J.* **2006**, *52*, 1877.
[50] I. Valente, E. Celasco, D. L. Marchisio, A. A. Barresi, *Chem. Eng. Sci.* **2012**, *77*, 217.
[51] D. V. Alexandrov, *Chem. Eng. Sci.* **2014**, *117*, 156.
[52] T. Brousse, D. Belanger, J. W. Long, *J. Electrochem. Soc.* **2015**, *162*, A5185.
[53] Y. Gogotsi, R. M. Penner, *ACS Nano* **2018**, *12*, 2081.
[54] M. Jing, H. Hou, C. E. Banks, Y. Yang, Y. Zhang, X. Ji, *ACS Appl. Mater. Interfaces* **2015**, *7*, 22741.
[55] C. Hao, L. Hu, C. Min, Y. Yan, L. Wu, *Adv. Funct. Mater.* **2014**, *24*, 6700.
[56] M. Nawwar, R. Poon, R. Chen, R. P. Sahu, I. K. Puri, I. Zhitomirsky, *Carbon Energy* **2019**, *1*, 124.
[57] W. Wang, Y. Lu, M. Zhao, R. Luo, Y. Yang, T. Peng, H. Yan, X. Liu, Y. Luo, *ACS Nano* **2019**, *13*, 12206.
[58] F. Guo, Y. Wu, H. Chen, Y. Liu, L. Yang, X. Ai, X. Zou, *Energy Environ. Sci.* **2019**, *12*, 684.
[59] N. Xu, G. Cao, Z. Chen, Q. Kang, H. Dai, P. Wang, *J. Mate. Chem. A* **2017**, *5*, 12379.
[60] F. Hu, H. Wang, Y. Zhang, X. Shen, X. Wu, Y. Xiong, Z. Peng, *Small* **2019**, *15*, 1901020.
[61] W. Hao, R. Wu, R. Zhang, Y. Ha, F. Fang, Y. Guo, *Adv. Energy Mater.* **2018**, *8*, 1801372.
[62] H. Chen, S. Ouyang, M. Zhao, Y. Li, J. Ye, *ACS Appl. Mater. Interfaces* **2017**, *9*, 40333.
[63] L. Wu, Q. Li, C. H. Wu, H. Zhu, A. Mendoza-Garcia, B. Shen, J. Guo, S. Sun, *J. Am. Chem. Soc.* **2015**, *137*, 7071.

[64] J. Masa, P. Weide, D. Peeters, I. Sinev, X. Wei, Z. Sun, C. Somsen, M. Muhler, W. Schuhmann, *Adv. Energy Mater.* **2016**, *6*, 1502313.
[65] J. Chang, Y. Xiao, M. Xiao, J. Ge, C. Liu, W. Xing, *ACS Catal.* **2015**, *5*, 6874.
[66] L. A. Stern, L. Feng, S. Fang, X. Hu, *Energy Environ. Sci.* **2015**, *8*, 2347.
[67] C. Xiang, Y. Liu, Y. Yin, P. Huang, Y. Zou, M. Fehse, Z. She, F. Xu, D. Banerjee, D. Hermida-Merino, *ACS Appl. Energy Mater.* **2019**, *2*, 3389.
[68] C. Yu, Y. Wang, J. Cui, D. Yu, X. Zhang, X. Shu, J. Zhang, Y. Zhang, R. Vajtai, P. M. Ajayan, Y. Wu, *J. Mater. Chem. A* **2018**, *6*, 8396.
[69] L. Liu, H. Yu, A. Liu, Y. Xu, B. Feng, F. Yang, P. Zhang, J. Wang, Q. Deng, Z. Zeng, S. Deng, *Electrochim. Acta* **2019**, *327*, 134970.
[70] H. Jia, Q. Li, C. Li, Y. Song, H. Zheng, J. Zhao, W. Zhang, X. Liu, Z. Liu, Y. Liu, *Chem. Eng. J.* **2018**, *354*, 254.
[71] X. Feng, Y. Huang, C. Li, X. Chen, S. Zhou, X. Gao, C. Chen, *Chem. Eng. J.* **2019**, *368*, 51.
[72] W. Xing, S. Qiao, X. Wu, X. Gao, J. Zhou, S. Zhao, S. B. Hartono, D. H. Jurcakova, *J. Power Sources* **2011**, *196*, 4123.